Journal Pre-proof

Active responses of nanoparticle-polymer interface/interphase via the interfacial interaction redistribution

Guotong Wang , Ruijie Wang , Chengyuan Wang , Chun Tang , Faling Zhang

PII: S0020-7403(22)00908-0
DOI: https://doi.org/10.1016/j.ijmecsci.2022.108030
Reference: MS 108030

To appear in: *International Journal of Mechanical Sciences*

Received date: 5 October 2022
Revised date: 28 November 2022
Accepted date: 10 December 2022

Please cite this article as: Guotong Wang , Ruijie Wang , Chengyuan Wang , Chun Tang , Faling Zhang , Active responses of nanoparticle-polymer interface/interphase via the interfacial interaction redistribution, *International Journal of Mechanical Sciences* (2022), doi: https://doi.org/10.1016/j.ijmecsci.2022.108030

Highlights

- A strain triggers the interaction redistribution and active interphase/face responses.
- Strain-dependent material properties are achieved for the stretched interphase.
- Highly nonlinear behavior with three statuses is found for the elongated interface.
- Physical parameters are defined for the interface subjected to general loadings.

Active responses of nanoparticle-polymer interface/interphase via the interfacial interaction redistribution

Guotong Wang[1], Ruijie Wang[1], Chengyuan Wang[2*], Chun Tang[1*], Faling Zhang[1]

1. Faculty of Civil Engineering and Mechanics, Jiangsu University, Zhenjiang 212013, China
2. Zienkiewicz Centre for Computational Engineering, Faculty of Science and Engineering, Swansea University, Bay Campus, Swansea, Wales SA1 8EN, UK

Abstract Physical responses of nanoparticle (NP)-polymer interphase/interface to external stimulus is a topic of great interest in nanocomposites. Previously, the interphase was tacitly assumed to have passive responses with constant material properties during deformation while the interface was mainly studied under hydrostatic loadings. To explore the unique features of the interphase we used a full-atom molecular dynamics simulation to monitor the evolution of its mass density and atomic stress profiles during deformation. A cohesive zone model was then used to define the key parameters for the NP-polymer interaction, which enable one to study the responses of the interface without spherical symmetry and understand the unique behavior of the stretched interphase/interface. The conceptual change has been achieved showing that an external strain can redistribute the NP-polymer interaction to affect

the high compression in the interphase, the physical origin of the interface confinement effect in the nanocomposite. This eventually triggers the active responses of the interphase leading to the apparent strain-dependence of the mass density and some other properties. The redistribution of the interfacial interaction also brings about the stable, metastable and unstable status of the stretched interface characterized by the strain-dependent modulus and interface debonding.

Keywords: nanoparticle-polymer interphase/interface, cohesive zone model, molecular dynamics simulations, strain-dependent density profile, nonlinear behavior.

Email: chengyuan.wang@swansea.ac.uk and tangchun@ujs.edu.cn

1. Introduction

In nanofiller (NF)-polymer composites [1-6], the large surface-to-volume ratio of the NFs enhances the effect of the NF-polymer interaction which separates the two components and changes the physical properties of the polymer in the vicinity of the NF-polymer interface. Two new phases are thus formed, i.e., the NF-polymer interface and interphase between the NF and bulk polymer. This unique feature gives rise to the emergence of the distinct behaviour/properties of the interface/interphase which will pass across the length scales to impact the material properties of the nanocomposites. The physical responses of the NP-polymer interface/interphase to external stimulus thus have attracted considerable attention from the community of nanocomposites [7-12].

For the interface between polymer and the various NFs, e.g., carbon nanotubes (CNTs) [13-16, 18, 19], nanosheets [13,16,18] and nanoparticles (NPs) [17,18,20], cohesive zone models were developed to study its responses to external loads. The closed form expressions for the cohesive energy and tensile stress were obtained for the interface at equilibrium state or subjected to external load [13-20]. In particular, good agreement has been achieved between the cohesive zone models and molecular dynamics (MD) simulations or experiments

[16, 18]. Based on the theory, the interface debonding and interface strength were discussed [15,17, 20] and importantly, major factors were identified in determining the interfacial interaction, interface strength and debonding strain, which include NF size, NF fraction, interface spacing and interphase properties [15, 16-20]. In existing studies, dilute solution assumption was normally used [14, 16, 17] and its applicable range was examined in [20]. Herein, it is noted that previous research on NP-polymer or nanotubes-polymer interface was focused on the spherically or cylindrically symmetric interface subjected to radial tensile stress [15-20]. The interface's responses to general loadings, e.g., uniaxial load, have not been studied in detail as it is difficult to capture the interface shape and calculate the cohesive energy and stress in the absence of spherical or cylindrical symmetry.

The interphase generated by the confinement effect of the interface [21-25] is another fundamental issue in nanocomposite. MD simulations and micro-mechanics models [27-39] were employed to examine the interphase/interface effect on the overall material properties of nanocomposites. The influence of interfacial interaction, the grafting ratio of the interfaces, the interphase properties and the geometric size were characterized for the elastic moduli, yield stress, fracture properties, thermal elastic properties, glass transition temperature and shear band location of the NP-based nanocomposites [8, 26-33]. The research on the interface/interphase effect was critically reviewed in Refs. [9, 12].

In the past two years, the interphase effects on the thermal and/or elastic properties were examined for the copper NP [34], α-graphyne nanotubes [35] and nanocones [36]-based nanocomposites. It was found that α-graphyne nanotubes are better nanofillers than CNTs due to their stronger interaction with polymer [35]. In addition, the size and properties of the inner interphase inside the nanocones were found to change with their geometries [36]. Furthermore, the influence of the interphase on the creep behavior was also studied for CNT or graphene reinforced nanocomposites [37-39]. The interphase behavior (e.g., viscous elastic

behavior) and its size were found to play an essential role in determining the creep responses and moduli of the nanocomposites [37-39]. Specifically, it was indicated that thicker and stiffer interphases lead to higher creep moduli for the graphene/epoxy nanocomposites [39].

Moreover, efforts were made to experimentally examine the confinement effect of the interface [40-45] and measure the physical properties of the interphase [46-50]. The nanoscale experiments however remain challenging due to the limitation of the currently available characterization techniques. As a result, computer simulations and mechanical models were used as an alternative means. Viscosity and fragility were studied for the confined polymer by combining polymer X-ray scattering based dynamics measurements and coarse-grained molecular dynamics (CGMD) simulations [51]. The emphasis was placed on the effects of long relaxation time of the confined polymer and the thickness of the interface. The interphase structure and dynamics (i.e., mobility of polymer chains) were also discussed for the NP-nanocomposite based on CGMD simulations [52]. More recently, the first principles calculation was used to probe the structural, conformational and dynamical properties of polymer chains in the proximity of both bare gold NP (AuNP) and functionalized AuNP [53].

The mechanical properties (e.g., elastic modulus, thermal-mechanical stability), peak mass density and orientation of the polymer chains of the interphase have also attracted considerable attention in recent studies [8-12, 34-36, 54-56]. It was noted that the interfacial covalent bonding and interface compliance are essential in determining the interphase properties [8-12]. Nonnegligible fluctuations was also observed for the interphase elasticity random field [54]. Furthermore, the correlation between the peak mass density and high pressure in the interphase was captured [55, 56]. Such high compression in the interphase is found to be a result of the NP-polymer interaction and the physical origin

from which the interface confinement effect has arisen [56]. For more comprehensive review on the studies of the interphase structure and material properties readers may refer to [12, 57].

In previous studies [10, 11, 15, 26, 36, 54, 55] it was tacitly assumed that the interphase like bulk materials exhibits passive responses with the material properties independent of deformation. This however may not be truth as the nanoscale material properties can have unique behavior different than those of bulk properties [58, 59]. In particular, the external loads may affect the high compression of the interphase [56] and lead to the variation of its mass density and other material properties. Thus, effort is urgently needed to examine this issue and bring new insight into the behavior of the interphase under mechanical loads.

The present study aims to resolve these issues in nanocomposite research by combining a cohesive zone model and MD simulations. A full atomic model of AuNP – polyethylene (PE) system was established and its mechanical responses under uniaxial load were studied. Herein, efforts were first made to calculate the mass density and stress profile for the elongated interphase in various radial directions. The correlation between them was observed and then analyzed theoretically. Subsequently, the cohesive zone model complemented by MD simulations was used to define the parameters for the interfacial interaction and characterize the interface response to uniaxial strain. The distinctive behavior of the interface was also studied in terms of the strain-dependent modulus, stain-induced redistribution of the interfacial interaction and the development process of the interface debonding.

2. Methodology

In this section, we shall demonstrate the modelling techniques used in the present study of AuNP-PE interphase/interface. MD simulation will be described in Sec.2.1 to introduce the AuNP-PE system studied, the potentials selected and the tensile test procedure for the

composite system. A cohesive zone model will then be introduced in Sec. 2.2 to derive the formulae of cohesive energy, force and stress of the NP-polymer interface under general loadings.

2.1 Molecular dynamics simulation

Herein, a full atomic model is employed to study the AuNP-PE composite, as a typical example of an NP-polymer system. To construct the initial representative volume element (RVE) of the AuNP-PE composite 500 monomer-long PE chains are continuously packed into a unit cell containing an AuNP of radius 2.5*nm* at its center until the mass density 0.46 g/cm^3 is obtained for the PE. This density is selected to avoid high-energy initial configurations. The obtained initial RVE contains 18 PE chains and 57961 atoms.

MD simulations in this study are conducted via the largescale Atomic/Molecular Massively Parallel Simulator (LAMMPS) [60]. The equations of motion for all simulations are integrated using the velocity Verlet algorithm with a time step of 1 *fs* and the periodic boundary conditions are used in all directions to eliminate the finite size effect. For the interaction potentials between atoms in the simulations, the COMPASS force field is employed for the description of PE chains, in which the terms of bond, angle, dihedral, bond-bond and bond-angle interaction among cross-coupling terms, and nonbonded interactions are considered in simulation [61]. As argued by H. Sun [61], these terms play a major role in determining the physical properties of polymer. We have demonstrated the reliability of this force field for the PE by comparing the simulation results with others in calculating mass density, Young's modulus and the glass transition temperature [56]. Embedded atom method (EAM) potential [62] and 12-6 Lennard-Jones (L-J) potential are utilized for describing the interaction between the Au atoms, and the Au and the PE atoms, respectively. The van der Waals (vdW) interactions are truncated at 1*nm* [63] and the values of its parameters are summarized in Table S1.

After achieving the initial RVE, a local energy minimum process is conducted under the employed potentials with maximum iterations up to 10^5 by the conjugate gradient method. Then a global energy minimum is implemented by a simulated annealing as follows: the system was initially thermalized at 500K for 1ns under the NVT ensemble and subsequently under the NPT ensemble at 0 atm for another 1ns. After that, the system is cooled down from 500K to 100K using NPT ensemble within a 2ns period. This is followed by final equilibration step of 2ns under the NPT ensemble. After such procedure, the volume fraction of AuNP obtained in the RVE varies from 6.5% to 12.1%. Such an annealing process is necessary to ensure that the equilibrated AuNP-PE system obtained holds structural properties in agreement with experimental and previous simulation data [32, 56].

A uniaxial tensile strain is then applied to the equilibrated AuNP-PE system at a temperature of 100K and a constant strain rate of 10^{-6} fs^{-1}. Here the uniaxial strain is realized via varying the periodic box size along the tensile direction at a constant rate, the coordinates of the atoms are rescaled accordingly so that there is no nonphysical interaction imposed between atoms and those of surrounding periodic cells. The pressure along directions normal to the tensile direction is kept 0 in order to consider the Poisson effect. Due to the periodic boundary conditions used, the AuNP-PE system can be considered as an isotropic nanocomposite with periodically dispersed NPs. Noted that, although an affine strain field is applied to the equilibrated AuNP-PE system during the deformation process, the presence of highly stiff NPs leads to a non-affine strain field in the sample. In the system, NPs practically do not experience any strain, but their presence alters the local strain within the polymer in the vicinity of the NP [54]. The entire tensile test is conducted under the NPT ensemble and the overall applied strain is up to 100%. To eliminate the uncertainty due to the initial condition effect, the virtual tests are performed for nine AuNP-PE systems with uncorrelated configurations, and the average values are used in Sec. 3.

2.2 Cohesive zone model for NP-polymer interface

To study the interaction between a NP and polymer under uniaxial tensile load, a cohesive zone model [17, 18, 20] is used, where, as shown in Fig. 1 (a), a spherical NP (yellow) is surrounded by the NP-polymer interface (the white gap between the NP and polymer due to vdW interaction), the interphase in polymer (the brown area) and the bulk polymer matrix (the gray area). In the figure, r_{NP} is the radius of the NP, r_e is the radial distance between the NP center and outer surface of the interface (OSI) (the red line in Fig. 1(a)), and r_b the radius of the spherical boundary of the polymer matrix. Note that the OSI is initially a spheric surface but can be of different shapes when being subjected to an external load. To further explain the structure of a NP-polymer system, we show the mass density profile of an AuNP-PE system in Fig. 1 (b) where the mass density $\varrho_m(r)$ of the interphase is a function of the distance r between the reference point and NP center. ϱ_m takes the bulk value ϱ_o at the OSI (i.e., $\varrho_m(r_e) = \varrho_o$), fluctuates around it in the interphase and finally approaches ϱ_o in the polymer matrix.

The vdW interaction between NP and polymer matrix is characterized by Lennard-Jones (L-J) potential function $V(r)$ where an attractive part is caused by dipole-dipole attraction and a short-range repulsive part is caused by Pauli's exclusion principle (Supporting Information S1). The cohesive energy between two differential elements of NP and polymer is $V(r) \cdot (\rho_{NP} dV_{NP}) \cdot (\rho_m dV_m)$ where ρ_{NP} and ρ_m are the volume densities of the NP and polymer, and dV_{NP} and dV_m are the volumes of the two differential elements. Here, $\rho_m = \varrho_m/\bar{m}$, $\bar{m}$ is the equivalent atomic mass of the polymer considered. The cohesive energy between $\rho_m dV_m$ and the whole spheric NP can then be evaluated by [17, 18, 20].

$$\mathrm{d}\Phi = (\rho_m dV_m) \int_0^{\pi} \int_0^{2\pi} \int_0^{r_{NP}} V(r) \cdot (\rho_{NP} dV_{NP})$$

$$= \rho_m dV_m \rho_{NP} \int_0^{\pi} \int_0^{2\pi} \int_0^{r_{NP}} V(r)\, r^2 sin\varphi d\varphi d\theta dr$$

$$= \rho_m dV_m \rho_{NP} \Phi_0(r) \tag{1}$$

The specific form of $\Phi_0(r)$ can be found in Supporting Information S1. In Fig. 1(a), a polymer cone (the dashed blue lines) along a radial direction r of the NP can be defined by a combination of (φ, θ) in a spherical polar system whose origin coincides with the NP center. The height of the cone is $r_b - r_e$ and the area of its base on the OSI is $dS = r_e sin\varphi d\theta \times r_e d\varphi$. Note that, in the spherical polar system $dV_m = r^2 sin\varphi d\varphi d\theta dr$, the cohesive energy between the NP and the differential polymer cone in radial direction can be obtained by

$$\begin{aligned} \mathrm{d}\Phi_r = E_r &= \int_{r_e}^{r_b} \rho_{NP} \rho_m(r) \cdot \Phi_0(r)\, dV_m \\ &= sin\varphi d\varphi d\theta \int_{r_e}^{r_b} \rho_m(r) \cdot r^2 \Phi_0(r) dr \end{aligned} \tag{2}$$

The NP-polymer interaction in the radial direction defined by (φ, θ) can then be characterized by an equivalent cohesive stress σ_{osi} on the OSI. Keep in mind that $\rho_m(r_e) = \rho_0$ we have

$$\sigma_{osi} = \left(\frac{dE_r}{dr_e}\right) / ds = -\rho_0 \rho_{NP} \Phi_0(r_e) \tag{3}$$

Eq. (3) shows that σ_{osi} is determined by r_e which is generally a function of (φ, θ) on the OSI.

Subsequently, the cohesive energy Φ_{int} and equivalent cohesive force F_{int} between the NP and whole polymer matrix, respectively, can be obtained based on Eq. (2) and Eq. (3) as follows

$$\begin{aligned} \Phi_{int} &= \int_0^{2\pi} \int_0^{\pi} \mathrm{d}\Phi_r \\ &= \rho_{NP} \int_0^{2\pi} \int_0^{\pi} \int_{r_e}^{r_b} \rho_m(r) \Phi_0(r)\, r^2 sin\varphi d\varphi d\theta dr \end{aligned} \tag{4}$$

$$\begin{aligned} F_{int} &= \int_0^{2\pi} \int_0^{\pi} \sigma_{osi}\, r_e^2 sin\varphi d\varphi d\theta \\ &= -\rho_0 \rho_{NP} \int_0^{2\pi} \int_0^{\pi} \Phi_0(r_e) r_e^2 sin\varphi d\varphi d\theta \end{aligned} \tag{5}$$

Here F_{int} is not a real force but an algebraic addition of σ_{osi} across the OSI. This term thus can be used to measure the vdW force between the NP and the surrounding polymer.

Next let us calculate the cohesive energy Φ_{osi} between the NP and the OSI. Based on MD

simulations the thickness of the OSI equals to $1\mathring{A}$. Similar to Eq. (1), Φ_{osi} between the NP and a differential area $dS = r_e sin\varphi d\theta \times r_e d\varphi$ can be calculated as

$$d\Phi_{Sur} = \left(\rho_0 dS \times 1\text{Å}\right) \cdot \rho_{NP} \cdot \Phi_0(r_e) = \rho_0 \rho_{NP} r_e^2 \Phi_0(r_e) sin\varphi d\varphi d\theta \times 1\text{Å} \quad (6)$$

Thus, the cohesive energy between the NP and the OSI can be represented by

$$\Phi_{osi} = \oiint d\Phi_{Sur} = \rho_0 \rho_{NP} \int_0^{2\pi} \int_0^{\pi} \Phi_0(r_e) r_e^2 sin\varphi d\varphi d\theta \quad (7)$$

In terms of magnitude, we have we have $\Phi_{osi} = -F_{int}$ based on Eqs. (5) and (7). Here, the formula obtained can be used for the NP-polymer interface subjected to different loads and thus of various contour shapes. In particular, as will be shown later, F_{int}, σ_{osi} and Φ_{osi} are independent of specific mass density distribution of polymer (See Sec. 3.1) and determined primarily by the contour shape of the OSI or the NP-polymer interface, which varies with the type and magnitude of external load (See Sec. 3.2).

3. Results and discussions

Herein the MD simulation demonstrated in Sec. 2.1 will be used to investigate the strain-induced variation of the mass density distribution in the interphase and understand the observations by calculating the changes in atomic stress profiles due to the strain (Sec. 3.1). The simulations will be further employed to capture the strain-induced changes in the configuration of the stretched interface. With this information the formulae derived in Sec.2.2 will be used to calculate the strain-dependence of cohesive energy and cohesive force of the interface and compare the results with corresponding MD simulations (Sec.3.2). Subsequently, the formulae complemented by the MD simulations will be utilized to study the nonlinear mechanical behavior of

the stretched interface and show the redistribution of the interfacial interaction due to the strain. The results will then be used to reveal the physical mechanisms of the interface debonding and the strain-dependent atomic stress and material properties found in the interphase region (Sec.3.3).

3.1 Physical changes of the NP-polymer interphase

Previous efforts [15, 17, 31, 36, 54, 57] were made to study the interphase between NP and polymer, where the interphase was tacitly assumed to have passive responses to external loads. Under this assumption, the interphase modulus was measured, which is independent of the load applied and distributes uniformly in circumferential direction. These studies are of importance as the interphase will eventually impact the material behavior and properties of the bulk nanocomposites via percolation process.

To further explore the material behavior in the interphase region, we have, based on the full-atom MD simulation, conducted a uniaxial tensile test for an AuNP-PE system where the tensile strain ε_x is applied along the *x* direction (Fig. 2 (a)). The stress-strain relation obtained is shown in Fig. 2 (b) in comparison with the stress-strain relation of pure PE. Here the axial stress σ_x grows with rising ε_x and reaches its maximum value 166 *MPa* at $\varepsilon_x = 8\%$. After the yield point, σ_x declines with growing ε_x until $\varepsilon_x = 38\%$. σ_x then remains nearly a constant at $\varepsilon_x > 38\%$, i.e., the effective modulus is nearly zero and the material is flowing without significant strain-hardening. The evolution of the interface contour shape is illustrated in Fig. 2 (c) to (h) at strain increasing from 0 to 20%.

Here we shall first focus our attention on the mass density profile of the interphase stretched by raising ε_x. As will be shown later, the OSI subjected to a uniaxial strain will become a rotational ellipsoid which is symmetric about the *x*-axis. The mass density thus should remain nearly constant on the circle obtained by intersecting the ellipsoidal OSI with a rotating cone represented by the red lines in Fig.3 (a). The position of such a circle on the

OSI can be labeled by the apex angle φ of the cone, which grows from 0 to $\frac{\pi}{2}$ and to π (Fig.3 (a)). Here the density profile is measured along the radial directions of the AuNP with φ rising from 0 to $\frac{\pi}{6}$, $\frac{\pi}{3}$ and $\frac{\pi}{2}$ (Fig.3 (a)). The smoothing spline interpolation is used and detailed in Supporting Information S2. The results are shown in Fig.3 (b), (c), (d) and (e), respectively, where ε_x rises from 0 to 15%. The corresponding curves obtained at the same radial direction but with fixed strain are plotted in Fig. 3 (f) to (i). In these figures, the smooth curves given by the spline functions are plotted, where various dots are used to distinguish the curves associated with different strains.

The MD simulation data from which the spline functions are derived are not shown here.

At $\varepsilon_x = 0$ Fig.3 shows nearly the same sinusoidal density profile in all radial directions considered, where two peak densities are found at around r = 2.8nm and 3.3nm, respectively. With increasing radial distance r, the density fluctuates with decreasing amplitude and finally approaches its bulk value 0.9g/cm^3 in PE matrix. The interphase thus is limited in a 0.8nm-range of r. The highest peak density is about 1.46g/cm^3 which is 62% higher than the bulk value. In this particular case, the interface (or the OSI) is a spherical surface, and the interphase density varies along the radial directions but remains constant in circumferential direction. These results are found to be consistent with the density profiles obtained in previous studies [34-36,55-57] for NP-polymer interphases when there is no external load applied.

When ε_x is applied in the x-direction, the interface elongates along the radial direction at $\varphi = 0$ and becomes a stretched surface. It is thus noted in Fig. 3 (b) and (f) that the two density peaks of the interphase move away from the AuNP and their heights decrease significantly with rising ε_x. The peak densities become quite close to the bulk value at $\varepsilon_x =$ 8% to 15%. Similar trend is observed in Fig. 3(c) and (g) at $\varphi = \frac{\pi}{6}$ but the strain-induced

displacements of the density peaks and the reduction of their heights are found to be smaller than those at $\varphi = 0$. This trend can still be observed but becomes much less pronounced when φ rises to $\frac{\pi}{3}$ (Fig. 3 (d) and (h)) and $\frac{\pi}{2}$ (Fig. 3 (e) and (i)).

These MD simulations clearly show that the interphase exhibits active responses to the uniaxial strain leading to the redistribution of the mass density in the radial direction. Such a strain effect turns out to be more and more significant when the radial direction is getting closer to the direction of the strain applied. Accordingly, at a given strain the mass density of the interphase distributes nonuniformly in the circumferential direction. In previous studies [17, 31, 54, 55], the elastic modulus obtained for the interphase with higher density was found to be significantly higher than its bulk value showing the dependence of the modulus on the density of polymer. The density-dependence of glassy transition temperature is also observed for bulk polymer [64, 65] and the interphase region of nanocomposites [21, 23, 56]. The denser material in the interphase may also lead to the change of the electron tunneling barrier which is essential for the electron transfer behavior at the nanoscale [66]. As a result, the decrease of interphase density due to rising strain will be accompanied by the strain-induced changes of other interphase properties and eventually lead to the strain-dependent mechanical, piezoresistive and other material properties of the bulk nanocomposites.

In what follows let us study the physical mechanisms behind the observed strain-dependence of interphase properties. In 2022, Reda et. al. [55], calculated both the density and atomic-stress profile of the NP-polymer interphase at $\varepsilon_x = 0$. The authors found a peak hydrostatic pressure in the interphase and concluded that it "will be strongly correlated with the local density and this will be reflected in its distribution". Consistent with this, our recent study [56] showed that such high compression is the mechanical response of the polymer to the interfacial vdW interaction. In particular, this peak compressive stress gives rise to the nanoconfinement effect of the interface leading to the peak density and upshift of T_g of the

interphase at $\varepsilon_x = 0$ [56]. To confirm the correlation between the peak compression and peak density in the stretched interphase we have calculated the atomic-stress profile in the tensile test. The method used can be found in Ref. [55]. The results at given ε_x are plotted in Fig. 4 (a), (b), (c) and (d) with φ equal to 0, $\frac{\pi}{6}$, $\frac{\pi}{3}$ and $\frac{\pi}{2}$, respectively (Fig.3 (a)). Here we take the compressive stress positive and the tensile stress negative.

It is seen from Fig.4 that at $\varepsilon_x = 0$ the atomic-stress also shows a sinusoid distribution in all the radial directions which looks quite similar to the density profiles in Fig. 3. Specifically, the two peak compressive stresses are located in the places quite close to the two density peaks. Once ε_x is applied, the two peak compressive stresses shift to the right of the figures (Fig. 4 (a) and (b)) and their magnitudes decrease significantly along the radial directions with $\varphi = 0$ or $\frac{\pi}{6}$. This trend becomes trivial or negligible when φ is raised to $\frac{\pi}{3}$ and $\frac{\pi}{2}$ (Fig. 4 (c) and (d)). The comparison between Figs. 3 and 4 shows that under uniaxial strain the density profile varies (Fig.3) in nearly the same way the stress profile changes (Fig.4). These simulation data thus show clear evidence that the peak density and peak compressive stress are closely related to each other, which suggests that the strain-dependent interphase properties are a result of the strain-induced change of the peak compression in the interphase.

The physical mechanism behind this observation can be understood via the changes of the free volume in the interphase, i.e., the volume of matrix that is not occupied by polymer chains. A peak compressive stress achieved in the interphase can significantly decrease the free volume and thus enhances the local mass density and make local polymer stiffer and harder, i.e., higher elastic modulus. The mobility of the polymer chains is also dictated by the availability of the free volume as the less free volume makes more polymer chains entangled but with less free space to move. The peak compression thus can restrain the mobility of the polymer chains by decreasing the free volume, which in turn improves the glass transition temperature T_g in the interphase. In the tensile test, raising the tensile strain decreases the

peak compression in the interphase (Fig. 3), which increases the free volume gradually and thus continuously decreases the peak density as well as elastic modulus and T_g in the interphase. As a result, the interphase properties vary significantly with the type and magnitude of the external loadings. Herein the mechanistic pathway of the tensile strain to impact the peak compressive stress is another important issue, which will be discussed later in Sec. 3.3.

Here it is worth mentioning that the passive mechanical model is unable to predict the sinusoid stress profile achieved by MD simulation even if the real density profile is taken into consideration. Thus, the stress and density sinusoid distribution and their variation with rising strain obtained in MD simulations reflect a series of active physical changes in the interphase region, which is triggered by the high compression in the interphase due to the interfacial interaction and implemented via the reorientation and redistribution of the polymer chains or changes in the free volume and occupied volume. This dynamic process remains unclear and deserves to be studied in more details in future.

3.2 Deformation of the NP-polymer interface

In the previous section we investigated the active responses of the interphase to tensile strain. Next, we shall further study the deformation of an NP-polymer interface subjected to a uniaxial strain to capture its shape evolution driven by the strain. The OSI marked by the red line are shown in Fig. 2 (c), (d), (e), (f) and (h) at ε_x = 0, 2.3%, 4.9%, 8%, 15% and 20%, respectively. In this process, the inner surface of the AuNP-PE interface (i.e., the AuNP surface) is always a spherical surface and the OSI maintains a smooth closed surface at $\varepsilon_x \leq$ 15%, Based on this understanding, in what follows when we discuss the deformation or the shape of the interface, we mean the deformation or the shape of the OSI. With rising ε_x the original spherical interface elongates along the x direction but contracts in the directions

perpendicular to the *x*-axis. In particular, the shape of the interface should be symmetric about the *x*-axis. It is therefore reasonable to assume that under ε_x the original spherical interface will transform into a rotational ellipsoid with the long semi-axis *a* in the *x* direction and the short semi-axis *b* in both *y* and *z* directions. The deformed interface (or OSI) can thus be described by Eq. (8) in the polar coordinate system shown in Fig.1.

$$\frac{(r_e cos\varphi)^2}{a^2} + \frac{(r_e sin\varphi cos\theta)^2}{b^2} + \frac{(r_e sin\varphi sin\theta)^2}{b^2} = 1 \tag{8}$$

When ε_x is raised from 0 to 15% the values of *a* and *b* are measured for the AuNP-PE interface obtained in MD simulations (see details in Supporting Information S2). The results are shown graphically in Fig.5 as functions of ε_x. The polynomial curve fitting to the MD simulation data is also shown in Fig.5 as a guidance. Here *a* is found to increase monotonically from 2.73 *nm* to 3.28 *nm* when ε_x is raised from 0 to 15%. In contrast, *b* is fluctuating slightly around its initial value 2.73 *nm* without significant change. This is because the high repulsive force between the AuNP and polymer can resist the significant reduction of the gap between the AuNP and surrounding polymer along the radial directions with $\varphi = \frac{\pi}{2}$.

Based on Eq. (8) and ε_x – dependence of *a* and *b* (Fig.5), Φ_{int} (Eq. (4)) and Φ_{osi} (Eq. (7)) are calculated against ε_x (solid lines) in Fig.6 (a) in comparison with the data obtained directly based on the full-atom MD simulations (dots). An excellent agreement is achieved between the ellipsoid model and MD simulation in calculating Φ_{osi} as both techniques account for the strain-induced shape change of the interface and the density variation along radial direction has no influence on Φ_{osi}. However discrepancy is found in the magnitude of Φ_{int} obtained by the two techniques primarily due to the density variation in the interphase, which is captured by the MD simulations but neglected in the ellipsoid model where a constant mass density ρ_0 is used to replace $\rho_m(r)$. Despite this, the two methods predict

nearly the same trend of Φ_{int} or the rate of change of Φ_{int} with ε_x, i.e., $\frac{\mathrm{d}\Phi_{int}}{\mathrm{d}\varepsilon_x}$.

From these results it follows that though the density function $\rho_m(r)$ keeps changing with ε_x the total cohesive energy $\Phi_{int} = \rho_{NP}\int_0^{2\pi}\int_0^{\pi}\int_{r_e}^{r_b}\rho_m(r)\Phi_0(r)\,r^2 sin\varphi d\varphi d\theta dr$ is still a continuous function of ε_x. Specifically, $\frac{\mathrm{d}\Phi_{int}}{\mathrm{d}\varepsilon_x}$ varies with the rising ε_x as the semi-axis *a* and *b* are the functions of ε_x (Fig. 5). $\frac{\mathrm{d}\Phi_{int}}{\mathrm{d}\varepsilon_x}$, however, is found to be independent of the specific density profile $\rho_m(r)$ at given ε_x (Fig. 6 (a)). To understand this, let us consider E_r (Eq. (2)), i.e., the cohesive energy along a specific radial direction. Based on Eq. (2) we have $\frac{dE_r}{d\varepsilon_x} = -\rho_0\rho_{NP}\Phi_0(r_e)ds\cdot\frac{dr_e}{d\varepsilon_x}$ showing that the rate of change of E_r with ε_x is entirely determined by the contour shape of the interface (or $r_e(\varepsilon_x)$) at the specific radial direction (Eq. (8)) but not affected by the density distribution $\rho_m(r)$ in that direction. Here Φ_{int} can be obtained by adding E_r in all radial directions across the OSI (Eq. (4)) and thus should exhibit the same behaviour as the that of E_r. Moreover, this rule should also apply for the cohesive radial stress σ_{osi} defined by $\left(\frac{dE_r}{dr_e}\right)/ds$ in Eq. (3), the total cohesive force F_{int} in Eq. (5) and the modulus $Y_{int} = \frac{\partial F_{int}}{\partial \varepsilon_x}$ that will be given in Eq. (9).

3.3 Nonlinear responses of the AuNP-PE interface

The ellipsoid model (Sec.3.1) combined with the cohesive zone model (Sec.2.2) enables us to study the responses of the NP-polymer interface to uniaxial strain. Fig. 6 (a) shows the strain-dependence of Φ_{int} (Eq. (4)) and Φ_{osi} (Eq. (7)). The cohesive force F_{int} (Eq. (5)) on the NP-polymer interface also varies with rising ε_x. Thus, the equivalent modulus Y_{int} of the interface can be defined by Eq. (9) to quantify the ability of the interface to resist deformation.

$$Y_{int} = \frac{\partial F_{int}}{\partial \varepsilon_x} = -\rho_m \rho_{NP} \int_0^{2\pi} \int_0^{\pi} \begin{bmatrix} r_e^2 \frac{d\Phi_0(r_e)}{dr_e} \\ +2r_e \Phi_0(r_e) \end{bmatrix} \begin{pmatrix} \frac{\partial r_e}{\partial a} \frac{\partial a}{\partial \varepsilon_x} \\ + \frac{\partial r_e}{\partial b} \frac{\partial b}{\partial \varepsilon_x} \end{pmatrix} sin\varphi d\varphi d\theta \quad (9)$$

Here $r_e = \frac{ab}{\sqrt{b^2 cos^2\varphi + a^2 sin^2\varphi}}$, $\frac{\partial r_e}{\partial a} = \frac{b^3 cos^2\varphi}{\sqrt[3]{b^2 cos^2\varphi + a^2 sin^2\varphi}}$ and $\frac{\partial r_e}{\partial b} = \frac{a^3 sin^2\varphi}{\sqrt[3]{b^2 cos^2\varphi + a^2 sin^2\varphi}}$ can be derived based on Eq. (8) and a, b, $\frac{\partial a}{\partial \varepsilon_x}$ and $\frac{\partial b}{\partial \varepsilon_x}$ at given strain can be obtained directly from the data in Fig.5. In Fig. 6 (b) F_{int} and Y_{int} are shown as the functions of ε_x.

Similar to the interphase mass density, σ_{osi} should also remain constant on the circle represented by the red line on the ellipsoidal OSI (Fig.3 (a)). Thus, calculating σ_{osi} on these circles as a function of φ can intuitively reveal its spatial distribution across the ellipsoidal OSI, and its redistribution induced by rising strain ε_x. These studies are of interest as they can bring in a deep understanding of the nonlinear responses of the interface, the growth of the interface debonding and particularly, the pathway of the tensile strain ε_x to reduce the high compression in the interphase (Sec.3.1). Here the results are illustrated in Fig. 7 (a) to (d) at ε_x = 2.3%, 4.9%, 8% and 15%, respectively. In what follows, we shall consider the following four different stages of the interface (or OSI) to describe its mechanical responses to the uniaxial strain ε_x.

(1) At $\varepsilon_x = 0$, i.e., the equilibrium state, the cohesive energy Φ_{int} (Fig. 6 (a)) has the minimum value and the corresponding cohesive force F_{int} (Fig. 6 (b)) is zero. In the meantime, the maximum cohesive energy $\Phi_{osi} = 0$ (Fig. 6 (a)) is achieved on the AuNP-PE interface.

(2) At $\varepsilon_x < 4.9\%$, it is seen from Fig. 6 that raising ε_x leads to higher Φ_{int} with $\frac{d^2\Phi_{int}}{d\varepsilon_x^2} > 0$ and stronger attractive force F_{int} ($F_{int} > 0$), i.e., the AuNP-PE interaction is intensified due to rising external strain. Φ_{osi} ($=-F_{int}$) however, declines monotonically. In this process, positive Y_{int} is obtained in Fig. 6 (b), which rises slightly at $\varepsilon_x < 0.5\%$ but declines drastically at larger ε_x. These results indicate that the AuNP-PE interface is in a stable status

and can efficiently resist the deformation of the interface. Such an ability quantified by Y_{int} however diminishes swiftly with rising strain.

In Fig, 7 (a), a dumbbell-shaped distribution is achieved for σ_{osi} at $\varepsilon_x = 2.3\%$. Here, the highest attractive σ_{osi} of 148 *MPa* is found around the two ends of the interface (i.e., $\varphi = 0$ or π). σ_{osi} then decreases when the reference point moves towards the inner section of the interface and turns out to be a repulsive stress in the middle of the interface (i.e., around $\varphi = \pi/2$). The uniaxial load thus is transferred from the PE matrix to the AuNP via the attractive force around the two ends of the ellipsoidal interface's long axis.

(3) At $\varepsilon_x = 4.9\%$, while Φ_{int} reaches a turning point with $\frac{d^2\Phi_{int}}{d\varepsilon_x^2} = 0$ (Fig. 6 (a)), F_{int} has achieved its maximum value around 7.9*nN* (Fig. 6 (b)). At the same time, Φ_{osi} ($= -F_{int}$) on the interface has reached its lowest value and Y_{int} becomes zero in Fig. 6 (b). These results indicate that the interface has reached its metastable status and lost its ability to resist the external strain. $\varepsilon_x = 4.9\%$ thus indicates the beginning of the interface debonding. ε_x = 4.9% and $F_{int} = 7.9\,nN$ obtained can thus be considered as the fracture strain and strength of the AuNP-PE interface under the uniaxial strain.

At this metastable status, the dumbbell-shaped σ_{osi}distribution (Fig. 7 (a)) has transformed into a butterfly-shaped distribution (Fig. 7 (b)). The results show that attractive σ_{osi} drops swiftly at the two ends of the interface (Fig. 7 (b)) where the gap between AuNP and PE grows gradually, and highest attractive σ_{osi} shifts from the two ends towards the inner section of the elongated interface. The maximum value 148*MPa* of the attractive σ_{osi} however remains unchanged in this process. Repulsive σ_{osi} also increases slightly in the middle of the interface. Here it can be seen from Fig. 7 (a) and (b) that at $\varepsilon_x < 4.9\%$ the attractive force $F_{int} = \oiint \sigma_{osi} dS$ increases (Fig. 6 (b)) with ε_x mainly because the interface area associated with the maximum σ_{osi} grows substantially. At the same time, Y_{int} generally decreases (Fig.

6 (b)) primarily due to the decreasing growth rate of the interface area with the maximum σ_{osi}.

(4) At $\varepsilon_x > 4.9\%$, with rising ε_x Φ_{int} grows with $\frac{d^2\Phi_{int}}{d\varepsilon_x^2} < 0$ (Fig. 6 (a)) and F_{int} declines and approaches an asymptotic value around 5.8*nN* at sufficiently high ε_x (Fig. 6 (b)). In the meantime, Y_{int} becomes negative and approaches zero at large strain, e.g., $\varepsilon_x > 10\%$ (Fig. 6 (b)). The results indicate that the interface is in an unstable status, which cannot resist the strain. In other words, the debonding grows on the interface and the external load cannot be efficiently transferred from the PE to the AuNP. The AuNP thus behaves as if it was an empty hole.

At this unstable status, the butterfly-shaped distribution of σ_{osi} obtained at $\varepsilon_x = 4.9\%$ (Fig. (b)) is flattened at $\varepsilon_x = 8\%$ (Fig. 7 (c)) and then transformed into a double flying disc-shaped distribution at $\varepsilon_x = 15\%$ (Fig. 7 (d)). From the redistribution of σ_{osi} we can see that the interface debonding starts at the metastable status ($\varepsilon_x = 4.9\%$) and spreads out into the inner section of the interface ($\varphi \approx \frac{\pi}{2}$) at the unstable status ($\varepsilon_x = 4.9\%$). Thus, consistent with the above theoretical analysis, we can understand intuitively from Fig. 7 (c) and (d) that at the unstable status, the interface cannot efficiently transfer the load to the AuNP along the *x*-direction where the strain is applied. On the other hand, no matter how high ε_x is F_{int} cannot be zero but approaches a nonzero value as the AuNP and surrounding PE will always be interacting with each other via the highest attractive σ_{osi} and repulsive σ_{osi} in the small area around the center of the ellipsoidal interface (i.e., $\varphi = \frac{\pi}{2}$).

To confirm the results, let us compare the AuNP-PE composite with pure PE in a tensile test in Fig. 2 (b). The elastic modulus of the AuNP-PE composite (around 2.72*GPa*) obtained at low strain (i.e., the stable interface) is higher than its counterpart of the pure PE (around 2.38*GPa*), whereas its yield strain and stress (8% and 160*MPa*) achieved in relatively high

strain (i.e., the unstable interface) are significantly lower than those (18.6% and 191MPa) of the pure PE. Furthermore, at $\varepsilon_x > 38\%$ pure PE elongates at a stress level (around 150MPa) much higher than the stress level (around 50MPa) at which the AuNP-PE composite stretches. This observation is attributable to the equivalent empty hole in the composite system, which substantially reduces the area that can withstand the external load.

Here we shall attempt to understand the physical mechanism underlying the strain-induced reduction of the peak compression shown in Fig. 4. Fig. 5 shows that the uniaxial strain can stretch the spherical interface into an ellipsoidal one whose long semi-axis a grows with rising strain. The strain thus can substantially redistribute the cohesive stress σ_{osi} on the OSI of the interface (Fig. 7). Here we first look at the radial directions with φ around 0 (e.g., $0 \leq \varphi \leq \frac{\pi}{6}$) or π (e.g., $\frac{5\pi}{6} \leq \varphi \leq \pi$) (see Fig. 7(b)). Fig. 7(c) and (d) show that when ε_x is raised to 8% to 15% the AuNP-PE interaction σ_{osi} is very weak or negligible in these radial directions. In other words, the interface debonding occurs in the areas. Thus, the tensile stress cannot be efficiently transferred from the PE matrix to the AuNP. In this case, the strain or stress in the PE of the local area (or the interphase) almost vanishes and thus, the peak compression (Fig. 4 (a) and (b)) and peak densities nearly disappear (Fig. 3 (b) and (c)) in the strain range of [8%, 15%]. Next let us consider the radial directions with φ around $\frac{\pi}{2}$ (see Fig. 7(b)). In these directions, Poisson ratio effect gradually raises the radial repulsive interaction between NP and polymer, i.e., negative σ_{osi} when ε_x rises to 15% (Fig.7 (a) to (d)). As a result, the peak compression (Fig. 4 (c) and (d)) and thus the peak densities (Fig. 3(d) to (e)) in the radial directions remains nearly unchanged despite that the PE in the local area is subjected to a tensile strain ε_x in the x direction. It is thus concluded that the reduction of the higher compression primarily arises from the strain-induced redistribution of the NP-polymer interaction shown in Fig.7.

4. Conclusions

This paper studies the physical changes of stretched NP-polymer interphase/interface where the spheric symmetry of the NP-polymer system is broken. Efforts are also made to uncover the rationale behind the distinctive features of the interphase/interface. The new findings are summarized as follows.

A uniaxial tensile strain leads to an ellipsoidal interface where the AuNP-PE gap along its long axis grows with rising strain. This results in the continuous redistribution of the interfacial interaction, which weakens the AuNP-PE vdW interaction and thus decreases the peak compression found in the equilibrium interphase. As the peak density of the interphase arises from the reduction of the free volume due to the peak compression, the uniaxial strain eventually decreases the peak density in the interphase and reshapes the density profiles in both radial and circumferential directions. For a similar reason, the elastic modulus, glassy transition temperature, and electron tunneling energy barrier of the interphase can also change with the rising strain. The interphase thus exhibits active responses to mechanical stimulus and the substantial strain-dependence of the physical properties due to the strain-induced interfacial interaction redistribution.

In the study of the behavior of the stretched interface, the cohesive energy Φ_{int}, cohesive force F_{int}, radial cohesive stress σ_{osi} and modulus Y_{int} are first defined for the NP-polymer interface subjected to general loadings. It is interesting to find that the cohesive energy Φ_{int} remains a continuous function of strain ε_x despite that the density profile keeps changing with rising strain. Specifically, the uniaxial strain changes F_{int}, σ_{osi} and Y_{int} primarily due to the strain-induced contour changes of the interface and the resulted redistribution of the interfacial interaction. It is however independent of the density profile changes with the rising strain.

Furthermore, the strain-induced redistribution of radial cohesive stress σ_{osi} results in highly nonlinear behavior of the interface with three distinct stages characterized by the strain-dependent modulus Y_{int}. Positive Y_{int} at low strain signifies the stable interface that transfers the external load from the PE to the NP via the attractive σ_{osi} around the two ends of the stretched interface. At a critical strain $\varepsilon_x = 4.9\%$, Y_{int} is zero indicating the metastable interface where the interface debonding starts around the two ends of the ellipsoidal interface. Y_{int} turns out to be negative at higher strain showing an unstable interface, where the attractive σ_{osi} shifts to the center and the interface debonding spread from the two sides of the ellipsoidal interface to its central part. The AuNP thus is unable to take external load and nearly equivalent to an empty hole.

Author Statement

Guotong Wang: Conceptualization, Methodology, Visualization, Formal analysis and investigation; **Ruijie Wang:** Visualization, Investigation, Writing-original draft preparation, Funding acquisition; **Chengyuan Wang:** Conceptualization, Supervision, Formal analysis and investigation, Writing - review and editing, Resources; **Chun Tang:** Conceptualization, Supervision, Writing - review and editing, Resources, Funding acquisition. **Faling Zhang:** Visualization, Investigation and editing.

Declaration of interests

☒ The authors declare that they have no known competing financial interests or personal relationships that could have appeared to influence the work reported in this paper.

Acknowledgments

This work was supported by the National Natural Science Foundation of China (Grant no. 12072134) and Jiangsu Funding Program for Excellent Postdoctoral Talent (Grant no. 2022ZB664)

Declaration of Competing Interest

The authors declare that they have no known competing financial interests or personal relationships that could have appeared to influence the work reported in this paper

References

[1] Kinloch IA, Suhr J, Lou J, Young RJ, Ajayan PM. Composites with carbon nanotubes and graphene: An outlook. Science 2018;362:547-553.

[2] Harito C, Bavykin DV, Yuliarto B, Dipojono HK, Walsh FC. Polymer nanocomposites having a high filler content: synthesis, structures, properties, and applications. Nanoscale 2019;11(11):4653-4682.

[3] Bailey EJ, Winey KI. Dynamics of polymer segments, polymer chains, and nanoparticles in polymer nanocomposite melts: A review. Progs. Polym. Sci. 2020;105:101242.

[4] Ajmal CM, Benny AP, Jeon W, Kim S, Kim SW, Baik S. In-situ reduced nonxidized copper nanoparticles in nanocomposites with extraordinary high electrical and thermal conductivity. Mater. Today 2021;48:59-71.

[5] Yavitt BM, Salatto D, Zhou YX, Huang ZX, Endoh M, Wiegart L, Bocharova V, Ribbe AE, Sokolov AP, Schweizer KS, Koga T. Collective Nanoparticle Dynamics Associated with Bridging Network Formation in Model Polymer Nanocomposites. ACS Nano 2021;15(7): 11501−11513.

[6] Yi J, Xianyu YL. Gold Nanomaterials-Implemented Wearable Sensors for Healthcare Applications. Adv. Funct. Mater. 2022;32(9):2113012.

[7] Ferdous SF, Sarker MF, Adnan A. Role of nanoparticle dispersion and filler-matrix interface on the matrix dominated failure of rigid C-60-PE nanocomposites: A molecular dynamics simulation study. Polymer 2013;54(10):2565-2576.

[8] Wang ZK, Lv Q, Chen SH, Li CL, Sun SQ, Hu SQ. Effect of Interfacial Bonding on Interphase Properties in SiO2/Epoxy Nanocomposite: A Molecular Dynamics Simulation Study. ACS Appl. Mater. Interfaces 2016;8(11):7499-7508.

[9] Kashfipour MA, Mehra N, Zhu J. A review on the role of interface in mechanical, thermal, and electrical properties of polymer composites. Adv. Compos. Hybrid. Mater. 2018;1: 415–439.

[10] Fankhänel J, Arash B, Rolfes R. Elastic interphase properties of nanoparticle/epoxy nanocomposites: A molecular dynamics study. Compos. Part B-Eng. 2019;176:107211.

[11] Yang S. Interface and interphase of nanocomposites tailored by covalent grafting of carbon nanotube: Hierarchical multiscale modeling. Int. J. Mech. Sci. 2022; 220:107160.

[12] Huang J, Zhou JJ, Liu MJ. Interphase in Polymer Nanocomposites. ACS Au 2022; 2: 280−291.

[13] Jiang LY, Huang Y, Jiang H, Ravichandran G, Gao H, Hwang KC, Liu B. A cohesive law for carbon nanotube/polymer interfaces based on the van der Waals force. J. Mech. Phys. Solids. 2006;54(11):2436-2452.

[14] Tan H, Jiang LY, Huang Y, Liu B, Hwang KC. The effect of van der Waals-based interface cohesive law on carbon nanotube-reinforced composite materials. Compos. Sci. Technol. 2007; 67(14):2941-2946.

[15] Zhang YC, Zhao JH, Jia Y, Mabrouki T, Gong YD, Wei N, Rabczuk T. An analytical solution on interface debonding for large diameter carbon nanotube-reinforced composite with functionally graded variation interphase. Compos. Struct. 2013;104:261-269.

[16] Zhao JH, Jiang JW, Jia Y, Guo WL, Rabczuk T. A theoretical analysis of cohesive energy

between carbon nanotubes, graphene and substrates. Carbon 2013; 57:108-119.

[17] Ben SD, Zhao JH, Rabczuk T. A theoretical analysis of interface debonding for coated sphere with functionally graded interphase. Compos. Struct. 2014;117;288-297.

[18] Zhao JH, Lu LX, Zhang ZL, Guo WL, Rabczuk T. Continuum modeling of the cohesive energy for the interfaces between films, spheres, coats and substrates. Comp. Mater. Sci. 2015;96:432-438.

[19] Liu X, Yanga QS, He XQ, Liew KM. Cohesive laws for van der Waals interactions of super carbon nanotube/polymer composites. Mech. Res. Commun. 2016;72:33–40.

[20] Wang Y, Wang CY, Wang GT, Wang RJ. Effect of the surface curvature and volume fraction of AuPs on the AuP-matrix interface. Comp. Mater. Sci. 2017;134:58-66.

[21] Barbier D, Brown D, Grillet AC, Neyertz S. Interface between End-Functionalized PEO Oligomers and a Silica Nanoparticle Studied by Molecular Dynamics Simulations. Macromolecules 2004; 37(12):4695–4710. 28

[22] Baschnagel J, Varnik F. Computer simulations of supercooled polymer melts in the bulk and in-confined geometry. J. Phys. Condens. Mat. 2005;17(32):851–953.

[23] Chen L, Zheng K, Tian XY, Hu K, Wang RX, Liu C, Li Y, Cui P. Double Glass Transitions and Interfacial Immobilized Layer in in-Situ-Synthesized Poly(vinyl alcohol)/Silica Nanocomposites. Macromolecules 2010;43(2):1076–1082.

[24] Napolitano S, Glynos E, Tito NB. Glass transition of polymers in bulk, confined geometries, and near interfaces. Rep. Prog. Phys. 2017;80(3):036602.

[25] Genix AC, Bocharova V, Carroll B, Lehmann M, Saito T, Krueger S, He LL, Dieudonne-George P, Sokolov AP, Oberdisse J. Understanding the Static Interfacial Polymer Layer by Exploring the Dispersion States of Nanocomposites. ACS Appl. Mater. Interfaces 2019;11(19):17863–17872.

[26] Odegard GM, Clancy TC, Gates TS. Modeling of the mechanical properties of

nanoparticle/polymer composites. Polymer 2005;46(2):553–562.

[27] Yang S, Cho M. Scale bridging method to characterize mechanical properties of nanoparticle/polymer nanocomposites. Appl. Phys. Lett. 2008;93(4):043111.

[28] Yu S, Yang S, Cho M. Multi-scale modeling of cross-linked epoxy nanocomposites. Polymer 2009;50(3):945–952.

[29] Choi J, Yu S, Yang S, Cho M. The glass transition and thermoelastic behavior of epoxy-based nanocomposites: A molecular dynamics study. Polymer 2011;52(22):5197–5203.

[30] Yang S, Choi J, Cho M. Elastic Stiffness and Filler Size Effect of Covalently Grafted Nanosilica Polyimide Composites: Molecular Dynamics Study. ACS Appl. Mater. Interfaces 2012;4(9):4792-4799.

[31] Choi J, Shin H, Yang S, Cho M. The influence of nanoparticle size on the mechanical properties of polymer nanocomposites and the associated interphase region: A multiscale approach. Comp. Struct. 2015;119: 365-376.

[32] Wang Y, Wang RJ, Wang CY, Yu XZ. AuNP-PE interface/phase and its effects on the tensile behaviour of AuNP-PE composites. J. Appl. Phys. 2018;123(21):214305.

[33] Yang ET, Ivancic RJS, Lin EY, Riggleman RA. Effect of polymer–nanoparticle interaction on strain localization in polymer nanopillars. Soft Matter 2020;16(37):8639-8646.

[34] Shahrokh A, Fakhrabadi MMS. Effects of copper nanoparticles on elastic and thermal properties of conductive polymer nanocomposites. Mech. Mater. 2021;160:103958.

[35] Najafi G, Mashhadi MM, Fakhrabadi MMS. Reinforcement of polymer nanocomposites by α-graphyne nanotubes: A multiscale simulation. Comput. Mater. Sci. 2021;194:11043.

[36] Taheri SS, Fakhrabadi MMS. Interphase effects on elastic properties of polymer nanocomposites reinforced by carbon nanocones. Comput. Mater. Sci. 2022;201:110910.

[37] Ansari R, Hassanzadeh-Aghdam MK. Micromechanical investigation of creep-recovery

behavior of carbon nanotube-reinforced polymer nanocomposites. Int. J. Mech. Sci. 2016;115-116:45–55.

[38] Hassanzadeh-Aghdama MK, Mahmoodia MJ, Ansarib R. Creep performance of CNT polymer nanocomposites -An emphasis on viscoelastic interphase and CNT agglomeration. Compos. Part B-Eng. 2019;168:274–281.

[39] Hassanzadeh-Aghdam MK. Evaluating the effective creep properties of graphene-reinforced polymer nanocomposites by a homogenization approach. Compos. Sci. Technol. 2021;209:108791.

[40] Choi WJ, Kim HJ, Yoon KH, Kwon OH, Hwang CI. Preparation and barrier property of poly(ethylene terephthalate)/clay nanocomposite using clay-supported catalyst. J. Appl. Polym. Sci. 2006;100(6):4875–4879.

[41] Tannenbaum R, Zubris M, David K, Ciprari D, Jacob K, Jasiuk I, Dan N. FTIR characterization of the reactive interface of cobalt oxide nanoparticles embedded in polymeric matrices. J. Phys. Chem. B 2006;110(5):2227–2232.

[42] Gong L, Kinloch IA, Young RJ, Riaz I, Jalil R, Novoselov KS. Interfacial stress transfer in a graphene monolayer nanocomposite. Adv. Mater. 2010;22(24):2694–2697.

[43] Zhang HB, Zheng WG, Yan Q, Jiang ZG, Yu ZZ. The effect of surface chemistry of graphene on rheological and electrical properties of polymethylmethacrylate composites. Carbon 2012;50(14):5117–5125.

[44] Liao K, Aoyama S, Abdala A, Macosko C. Does graphene change T-g of nanocomposites? Macromolecules 2014;47(23):8311–8319.

[45] Liu Y, Hamon AL, Haghi-Ashtiani P, Reiss T, Fan B, He D, Bai J. Quantitative study of interface/interphase in epoxy/graphene-based nanocomposites by combining STEM and EELS. ACS Appl. Mater. Interfaces 2016;8(49):34151–34158.

[46] Hariharan R, Russel WB. Enhanced colloidal stabilization via adsorption of diblock

copolymer from a nonselective ϑ solvent. Langmuir 1998;14(25):7104–7111.

[47] Tadd E, Zeno A, Zubris M, Dan N, Tannenbaum R. Adsorption and polymer film formation on metal nanoclusters. Macromolecules 2003;36(17):6497–6502.

[48] Tannenbaum R, King S, Lecy J, Tirrell M, Potts L. Infrared study of the kinetics and mechanism of adsorption of acrylic polymers on alumina surfaces. Langmuir 2004;20(11):4507–4514.

[49] Wang SJ, Luo Z, Liang JJ, Hu J, Jiang NS, He JL, Li Q. Polymer Nanocomposite Dielectrics: Understanding the Matrix/Particle Interface. ACS Nano 2022;16(9):13612–13656.

[50] Cheng S, Bocharova V, Belianinov A, Xiong S, Kisliuk A, Somnath S, Holt AP, Ovchinnikova OS, Jesse S, Martin HJ, Etampawala TN, Dadmun MD, Sokolov AP. Unraveling the mechanism of nanoscale mechanical reinforcement in glassy polymer nanocomposites. Nano Lett. 2016;16(6):3630–3637.

[51] Das N, Begam N, Ibrahim M, Chandran S, Padmanabhan V, Sprung M, Basu JK. Viscosity and Fragility of Confined Polymer Nanocomposites: A Tale of Two Interfaces. Nanoscale 2019;11:8546-8553.

[52] Zhang WG, Emamy H, Betancourt BAP, Vargas-Lara F, Starr FW, Douglas JF. The interfacial zone in thin polymer films and around nanoparticles in polymer nanocomposites. J. Chem. Phys. 2019;151(12):124705.

[53] Power AJ, Remediakis IN, Harmandaris V. Interface and Interphase in Polymer Nanocomposites with Bare and Core-Shell Gold Nanoparticles. Polymer 2021;13(4):541.

[54] Le TT, Guilleminot J, Soize C. Stochastic continuum modeling of random interphases from atomistic simulations. Application to a polymer nanocomposite. Comput. Methods. Appl. Mech. Engrg. 2016; 303:430-449.

[55] Reda H, Chazirakis A, Behbahani AF, Savva N, Harmandaris V. Mechanical properties of

glassy polymer nanocomposites via atomistic and continuum models: The role of interphases. Comput. Methods. Appl. Mech. Engrg. 2022;395:114905.

[56] Wang GT, Wang RJ, Wang CY, Tang C, Luo Y, Xiao DH. Mechanistic pathway of NP-polymer interface to engender nanoscale confinement. Compos. Commun. 2022;32:101186.

[57] Sattar MA. Interface Structure and Dynamics in Polymer-Nanoparticle Hybrids: A Review on Molecular Mechanisms Underlying the Improved Interfaces. Chemistry Select 2021;6(20):5068–5096.

[58] Wang RJ, Wang CY, Feng YT. Effective geometric size and bond-loss effect in nanoelasticity of GaN nanowires, Int. J. Mech. Sci. 2017;130:267-273.

[59] Wang RJ, Wang CY, Feng YT, Tang C. Mechanisms underlying the shape effect on nano-piezoelectricity. Nano Energy 2018;53: 906-915.

[60] Plimpton S. Fast Parallel Algorithms for Short-Range Molecular Dynamics. J. Comput. Phys. 1995;117(1):1-19.

[61] Sun H. COMPASS: An ab Initio Force-Field Optimized for Condensed-Phase Applications ─ Overview with Details on Alkane and Benzene Compounds. J. Phys. Chem. B 1998;102(38):7338-7364.

[62] Foiles SM, Baskes MI, Daw MS. Erratum: Embedded-atom-method functions for the FCC metals Cu, Ag, Au, Ni, Pd, Pt, and their alloys. Phys. Rev. B 1988;37(17):10378.

[63] Hossain D, Tschopp MA, Ward DK, Bouvard JL, Wang P, Horstemeyer MF. Molecular dynamics simulations of deformation mechanisms of amorphous polyethylene. Polymer 2010;51(25):6071–6083.

[64] Bandi S, Schiraldi DA. Glass transition behavior of clay aerogel/poly(vinyl alcohol) composites. Macromolecules 2006;39(19):6537–6545.

[65] Pionteck J. Determination of Pressure Dependence of Polymer Phase Transitions by pVT

Analysis. Polymers 2018;10(6):578.

[66] Wang GT, Wang CY, Zhang FL, Yu XZ. Electrical percolation of nanoparticle-polymer composites. Compute. Mater. Sci. 2018;150 (8):102-106.

Figure

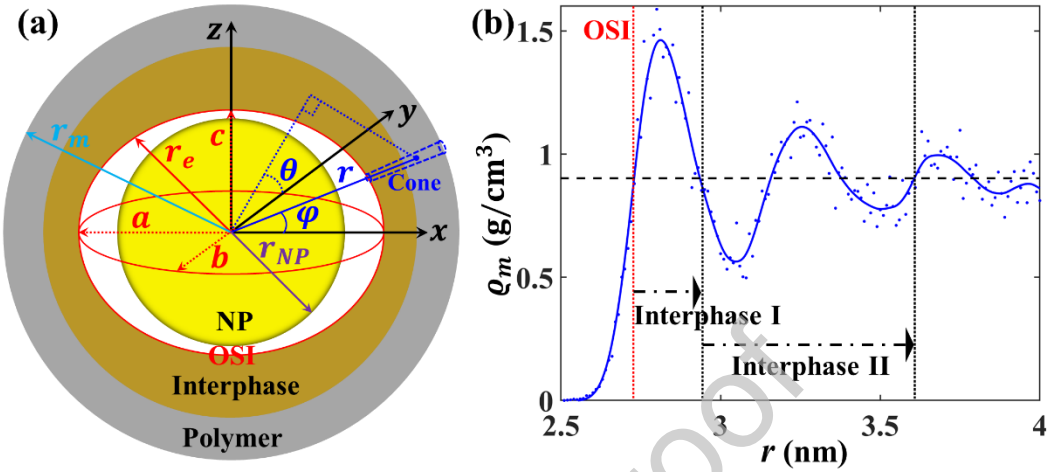

Fig.1 (a) The x-y-z coordinate system and mechanical model of an NP-polymer system where the yellow sphere is the NP and the white, brown, and grey areas are the NP-polymer interface, the interphase and bulk polymer. Here r_{NP} is the radius of the NP and r_e and r_m are the radial distance between the NP center (i.e., the origin of the *xyz* coordinate) and a point on the outer surface of the interface (OSI) and the bulk polymer, respectively. In addition, r indicates the radial direction of the NP, φ is the angle between the r and x directions, and θ is the angle between y-axis and the projection of the r direction on the zy plane. a, b and c are the semi axes of the ellipsoidal OSI in the x, y and z directions, respectively. Initially, the OSI is a sphere with $a = b = c$. When a tensile strain is applied in the x direction, we have $a > c = b$. (b) The r (radial) distribution of the mass density obtained for the PE in the vicinity of the interface when no external load is applied. The NP surface is at $r = 2.5nm$ and the position of the OSI is found at the place where the density first reaches its bulk value 0.94 g/cm^3. Moreover, the interphase has been divided into two regions, i.e., interphases I and II as shown in (b).

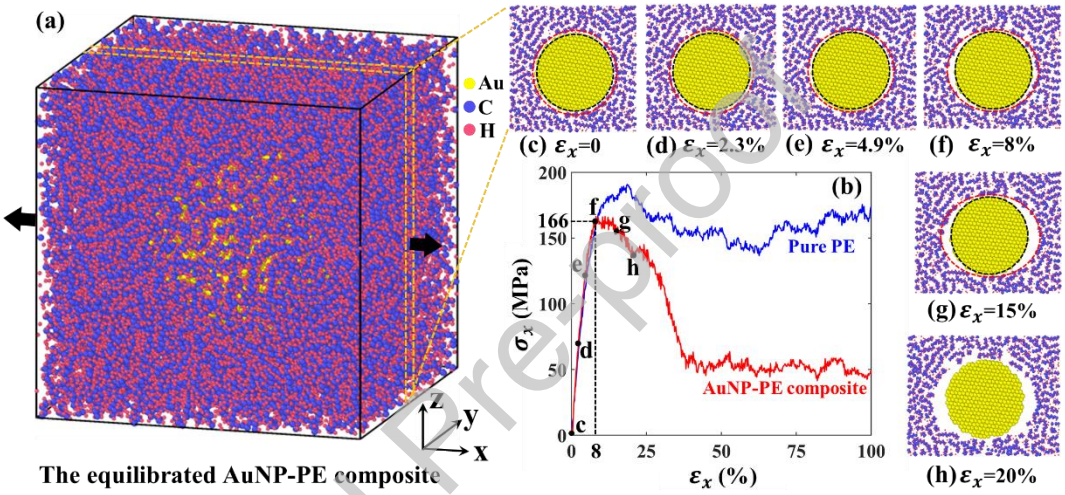

Fig. 2 (a) An AuNP-PE composite system in the *x*-*y*-*z* coordinator system, which is subjected to uniaxial tensile strain in the *x* direction. (b) Stress-strain relations obtained for the AuNP-PE composite system in the tensile test in comparison with its counterpart of pure PE system. The details of simulation for pure PE system can be found in Supporting Information S3. The shapes of the AuNP-PE interface (or the OSI) observed at points c, d, e, f, g, and h in (b) are shown in (c), (d), (e), (f), (g) and (h) where ε_x rises from 0 to 20%.

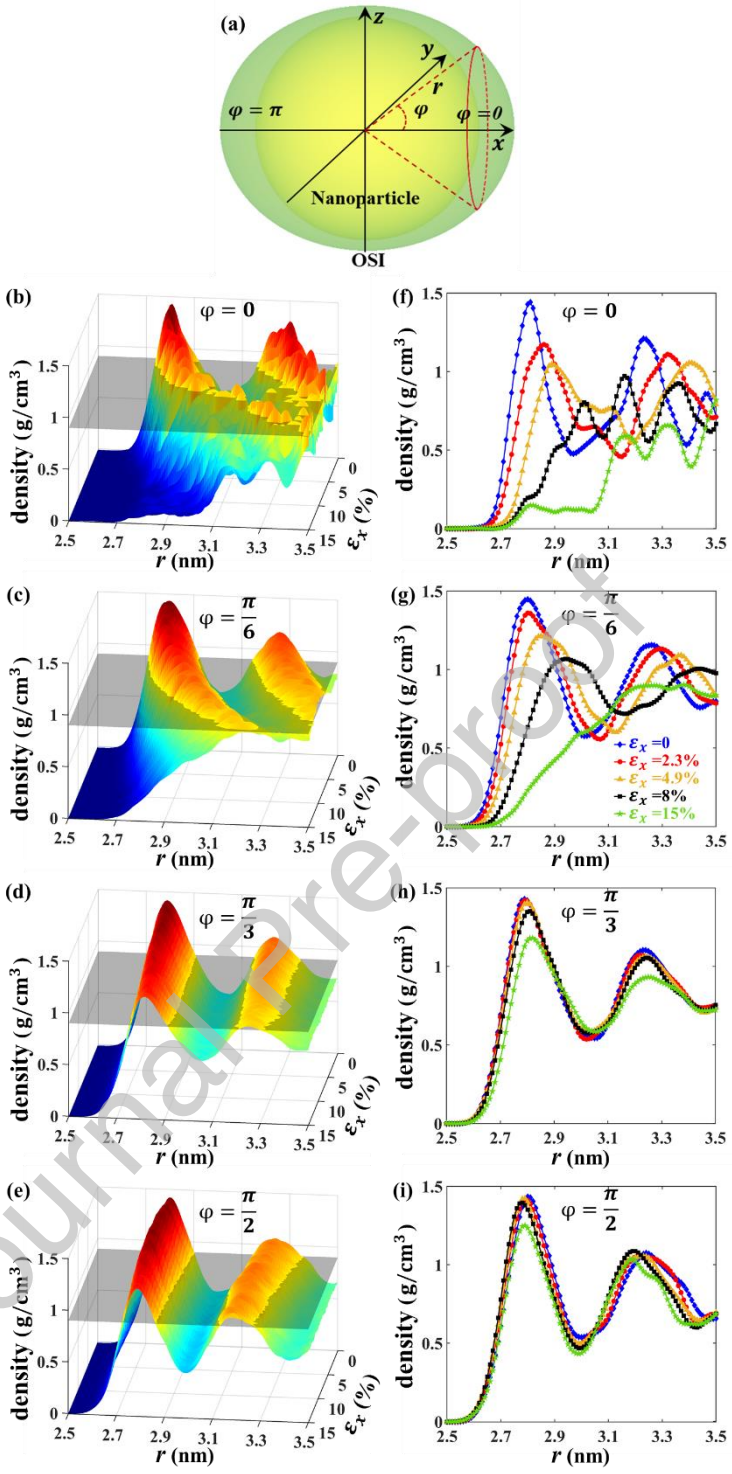

Fig.3 (a) The ellipsoidal AuNP-PE interface, the NP and a cone (red dashed lines) having an apex angle φ with the *x*-axis. The radial directions *r* of the NP can thus be labeled by φ rising from 0 to $\frac{\pi}{2}$ and π. (b-e) the density profile of the PE along the radial directions *r* of the AuNP with φ rising from 0 to $\frac{\pi}{6}$, $\frac{\pi}{3}$ and $\frac{\pi}{2}$ and ε_x growing from 0 to 15%, (f-i) the corresponding density profiles of the PE measured at the four radial directions and five fixed

strains.

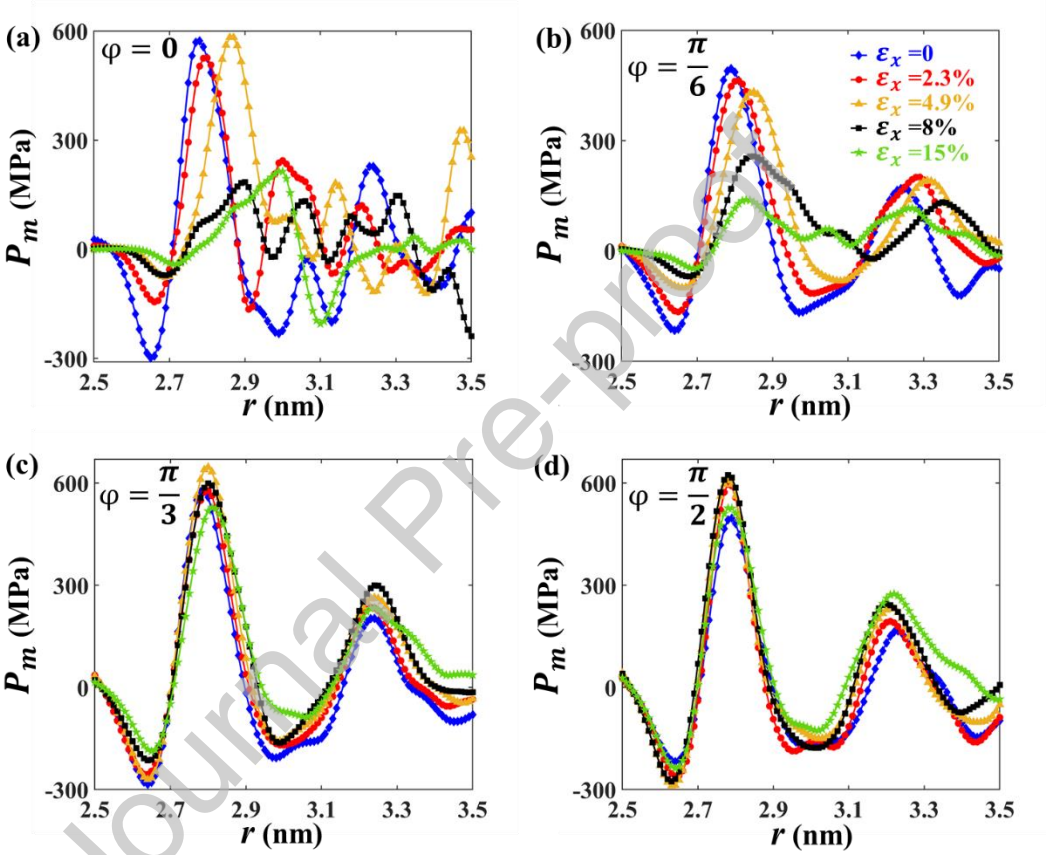

Fig.4 (a)-(d) Distribution of the atomic stress P_m measured in the PE interphase along various radial directions of the AuNP characterized by φ = 0, $\frac{\pi}{6}$, $\frac{\pi}{3}$ and $\frac{\pi}{2}$, respectively, when the uniaxial strain ε_x applied to the interface is fixed at 2.3%, 4.9%, 8% and 20%, respectively, as shown in (b).

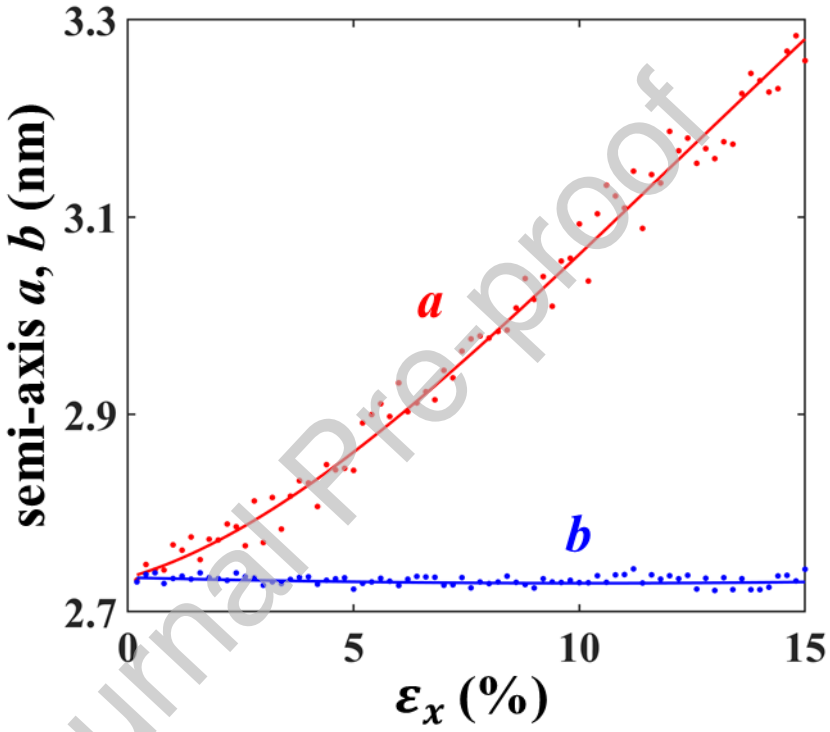

Fig.5 The strain ε_x-dependence of the long semi-axis a and short semi-axis b of the ellipsoidal outer surface of the AuNP-PE interface (see Fig. 1(a)) obtained by the MD simulations (dots) at $\varepsilon_x \leq 15\%$. The polynomial curve (solid line) fitting to the MD simulation data is also shown as a guidance.

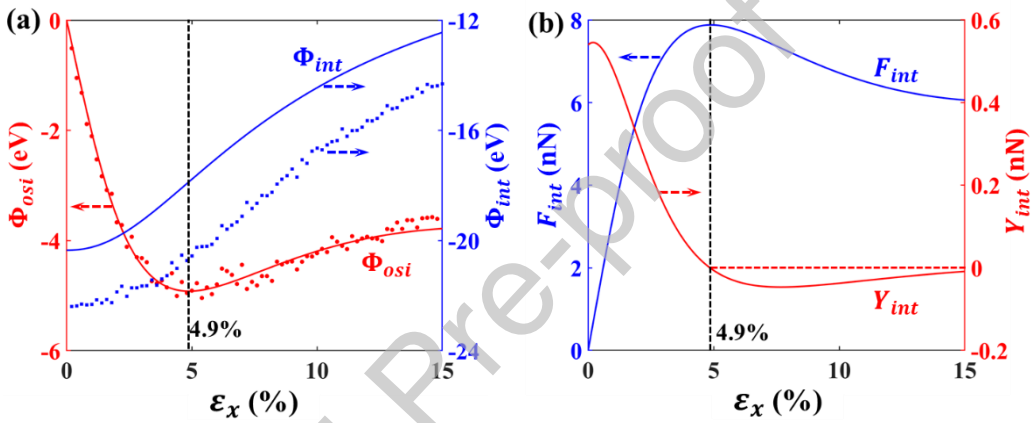

Fig.6 Strain ε_x-dependence of (a) cohesive energy Φ_{int} of the AuNP-PE interface and the cohesive energy Φ_{osi} on the outer surface of the interface (or the OSI), Here the results given by the cohesive model (solid lines) are compared with the MD simulation data (dots). (b) cohesive force F_{int} and tensile modulus Y_{int} of the AuNP-PE interface obtained based on the cohesive model. $\varepsilon_x = 4.9\%$ is the critical strain obtained at the metastable state of the interface.

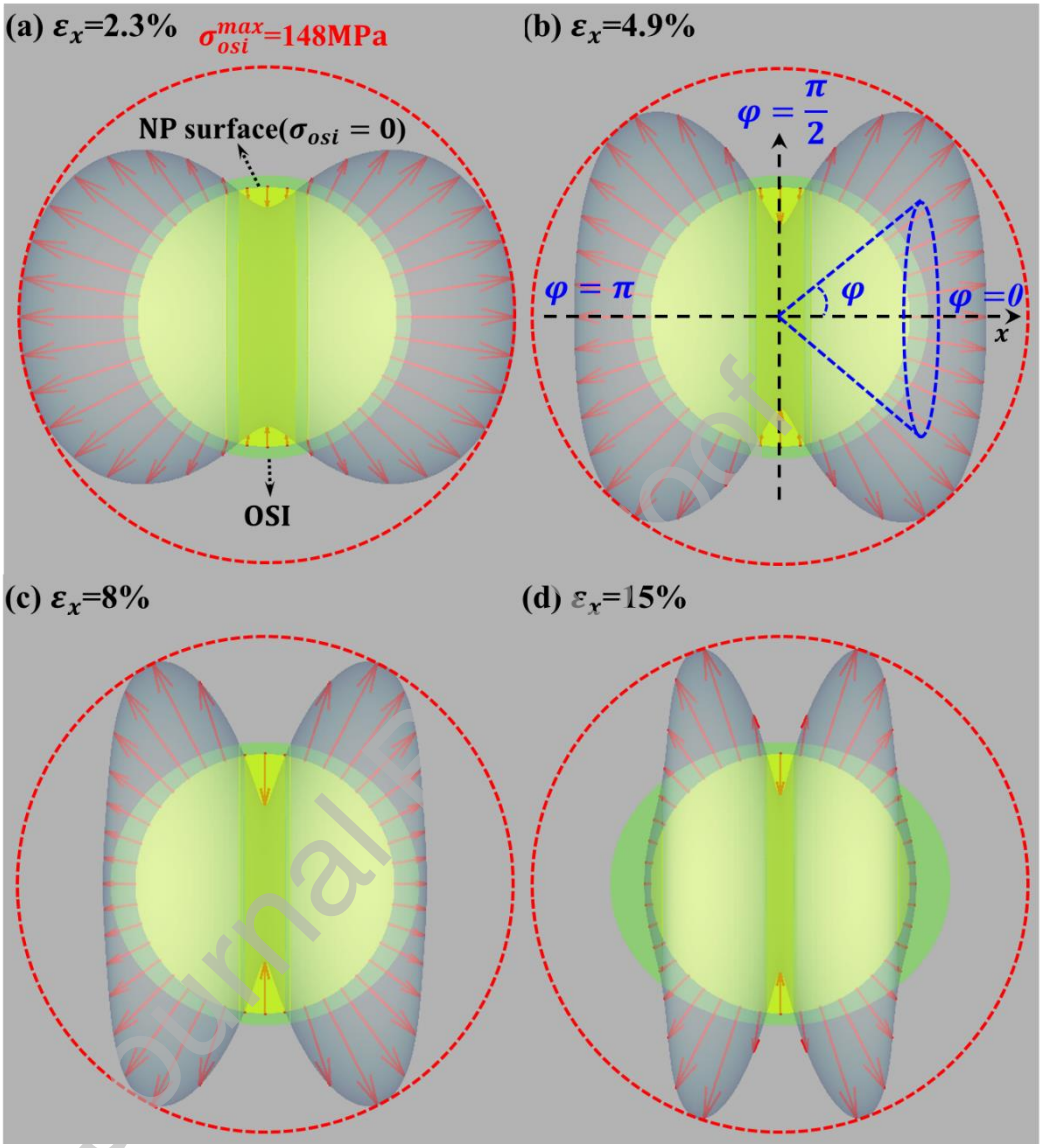

Fig.7 The gray envelop curves of the red arrows describe the distribution of the radial cohesive stress σ_{osi} on the OSI obtained at (a) $\varepsilon_x = 2.3\%$ (dumbbell-shaped), (b) $\varepsilon_x = 4.9\%$ (butterfly-shaped), (c) $\varepsilon_x = 8\%$ (flattened butterfly-shaped) and (d) $\varepsilon_x = 15\%$ (double-flying-disc-shaped), respectively. As shown in (a), the inner circle (yellow) and the outer ellipsoid (light yellow) represent the AuNP surface and the OSI, respectively. The large red circle and the inner yellow circle give the maximum stress $\sigma_{osi} = 148MPa$ and $\sigma_{osi} = 0$, respectively. In addition, the outward arrows denote the attractive force between the AuNP and PE, i.e., positive σ_{osi} and the inward arrows represent the repulsive force between them, i.e., negative

σ_{osi}.

Graphical Abstract